



ELSEVIER

Available online at [www.sciencedirect.com](http://www.sciencedirect.com)

SCIENCE @ DIRECT®

International Journal of Solids and Structures 43 (2006) 53–73

INTERNATIONAL JOURNAL OF  
**SOLIDS and  
STRUCTURES**

[www.elsevier.com/locate/ijsolstr](http://www.elsevier.com/locate/ijsolstr)

## Deformation rate effects on failure modes of open-cell Al foams and textile cellular materials

Sungsoo Lee <sup>a</sup>, François Barthelat <sup>a</sup>, Nicolaie Moldovan <sup>a</sup>,  
Horacio D. Espinosa <sup>a,\*</sup>, Haydn N.G. Wadley <sup>b</sup>

<sup>a</sup> Department of Mechanical Engineering, Northwestern University, 2145 Sheridan Road, Evanston, IL 60208, USA

<sup>b</sup> Department of Materials Science and Engineering, University of Virginia, 116 Engineer's Way, Charlottesville, VA 22904, USA

Received 8 August 2004; received in revised form 30 June 2005

Available online 1 September 2005

---

### Abstract

The compressive behavior of open-cell aluminum alloy foam and stainless steel woven textile core materials have been investigated at three different deformation rate regimes. Quasi-static compressive tests were performed using a miniature loading frame, intermediate rates were achieved using a stored energy Kolsky bar, and high strain rate tests were performed using a light gas gun.

In agreement with previous studies on foam materials, the strain rate was not found to have a significant effect on the *plateau* stress of metallic foams. For all the tests, *real time* imaging of the specimen combined with digital image correlation analysis allowed the determination of local deformation fields and failure modes. For the Kolsky bar tests, the deformations in the foam specimen were found to be more distributed than for the quasi-static test, which is attributed to moderate inertia effects. The differences in failure mode are more dramatic for the gas gun experiments, where a full compaction shock wave is generated at the impact surface. The stresses in front and behind the shock wave front were determined by means of direct and reverse gas gun impact tests, i.e., stationary and launched specimen, respectively. A one-dimensional shock wave model based on an idealized foam behavior is employed to gain insight into the stress history measurements. We show that the predictions of the model are consistent with the experimental observations. Woven textile materials exhibited moderate dependence of strength on the deformation rate in comparison with open-cell foam materials.

© 2005 Elsevier Ltd. All rights reserved.

*Keywords:* Metallic cellular materials; Dynamic compression; Aluminum foams; Woven textile lattice

---

\* Corresponding author. Tel.: +1 847 467 5989; fax: +1 847 491 3915.  
E-mail address: [espinosa@northwestern.edu](mailto:espinosa@northwestern.edu) (H.D. Espinosa).

## 1. Introduction

Materials combining lightweight and high mechanical energy absorption are of attracting interest for a variety of automotive, locomotive, marine, and aerospace applications (Gibson and Ashby, 1997; Ashby et al., 2000). Recent advances in materials fabrication and processing have led to the emergence of (stochastic) metal foams and truss lattices such as those made by metal textile routes. They are of interest because they combine low densities and high efficiency in absorbing mechanical energy from external loading. For this reason, research on metal foams and periodic cellular materials has been widely reported in the context of minimum weight design, advances in manufacturing, mechanical characterization, structural integrity, and large-scale simulations.

Among these efforts, experimental studies providing fundamental understanding of the mechanical behavior of these materials has been of paramount importance. Quasi-static tests have been well reconciled with models of foams that count for ligament bending. Those for periodic cellular materials have addressed plastic yielding and inelastic truss buckling. It appears that the dynamic response of these materials is significantly different from that measured under quasi-static conditions due to material strain rate dependence, micro-inertia (resistance to non-uniform velocities fields), and shock wave generation and propagation effects at high speeds of deformation.

Yi et al. (2001) reported a significant strain rate effect upon the compressive stress–strain curve of open-cell aluminum foams. By contrast, Dannemann and Lankford (2000), and Yu et al. (2003), who experimentally investigated the response and failure of dynamically loaded open- and closed-cell aluminum foams, using a Hopkinson bar techniques, did not observe any substantial rate dependency of the so-called plateau stress. By launching the specimen, Reid and co-workers (Reid and Peng, 1997; Harrigan et al., 1999; Tan et al., 2002) measured the force history at the impact surface and observed significant enhancements of strength under impact loadings. They proposed a model for shock waves in cellular structures to explain the strength enhancement. Following these ideas, Deshpande and Fleck (2000) conducted direct impact tests and measured the force applied to the specimen at the impact surface. In contrast to Reid and co-workers, they did not measure a strength increase as a function of deformation rate. However, their impact velocities were lower than the critical impact velocity required for the development of a shock wave. It could be conjectured that these discrepancies can be explained by changes in deformation and failure modes when a crushing shock wave is formed within a specimen loaded at very high deformation velocities. When a propagating discontinuity is present in a sample, the forces at the specimen ends are not balanced and determining the stress jump across the discontinuity requires two different experiments. Another potential source of deformation rate dependency is microinertia. Tam and Calladine (1991), and Reid and co-workers (Su et al., 1995a,b) studied plate structures and observed the structures exhibit an increase in strength with deformation rate. They proposed that inertia effects are a significant contribution to this rate effect even when the strain rate sensitivity of material properties is ignored. Crushing a foam involves significant motion of cell walls and ligaments within the material, whose inertia contributes to the overall compressive resistance. These phenomena have been hypothesized and modeled but not directly observed in *real time* on cellular materials. We also examine these issues.

Previous studies on the behavior of cellular materials have been mainly performed on foam materials with randomly shaped and distributed cells. Newly proposed approaches utilize metallic core materials which are topologically structured at small scale. Sypeck and Wadley (2001) developed metallic woven textile cores. The design and fabrication of the textile cores is reported in Sypeck and Wadley (2001), Wadley (2002), and Wadley et al. (2003). Theoretical and numerical analysis on the textile cores were performed by Wadley et al. (2003) and design optimization was pursued by Zok et al. (2003). Compression, shear, and bending experiments were carried out on the textile cores by Sypeck and Wadley (2001), Mumm et al. (submitted for publication), and Zupan et al. (2004) in quasi-static loading conditions. Whereas these textile

cores were studied theoretically and numerically, limited experimental data was reported and the performed experiments were limited to quasi-static loading.

This paper presents results from experiments on aluminum open-cell foams and stainless steel lattice truss structures made by the route. We report observations of their deformation at three different deformation rates. Quasi-static tests were performed on a miniature loading frame, intermediate strain rate tests were conducted using a stored energy Kolsky bar and high strain rate compression tests were performed using a gas gun. In addition to compressive stress–strain curves at various strain rates, real-time observations were made in all tests by means of digital high-speed imaging. Digital image correlation techniques were used to reveal deformation modes and inertia effects. The results are compared for all the explored deformation rates and conclusions are drawn for each material system. A one-dimensional shock wave model based on a rate independent, rigid-perfectly plastic locking idealization of the nominal stress–strain curve of the foam is examined and compared to the experimental data. The attributes and limitations of the model are highlighted.

## 2. Experimental techniques

The following sections provide details of the experimental setups and procedures employed in quasi-static, Kolsky bar and light gas gun compression tests. The gas gun setup was designed to test unit cells identical to those used in quasi-static and Kolsky bar experiments. The details of this new configuration are reported here for the first time.

### 2.1. Quasi-static experiments

Fig. 1 shows the experimental setup for the quasi-static compression test, where a strain rate in the order of  $10^{-3} \text{ s}^{-1}$  is achieved. The specimen was placed in a miniature loading stage (Ernest F. Fullam, Inc., Latham, NY) mounted with compression platens. A load cell was installed on the loading axis at the back of one compression platen. The compression load was measured by the 8896 N load cell connected to a PC via a signal processing unit and then the load signal was recorded using LabVIEW software (National Instruments, Austin, TX). The nominal stress was calculated by

$$\sigma_N(t) = F(t)/A_0 \quad (1)$$

where  $F(t)$  is the measured force and  $A_0$  is the initial cross-sectional area of the specimen. The setup was positioned under a 3-CCD camera (Hitachi Denshi America, Ltd., Woodbury, NY) equipped with a macro photographic lens (Navitar Inc., Rochester, NY). While the specimen was compressed, the load was recorded and sequential pictures of the deforming specimen were acquired synchronously to correlate the measurements of load and deformation at the same instance. The pictures captured from the movie were processed later to determine the displacements and strains using digital image correlation (DIC) schemes. This numerical method uses the distribution of intensities in the neighborhood of a pixel in the image to determine its displacement from one image to another. Repeating over several subsets the technique yields full field displacements with sub-pixel accuracy. Details on the method can be found elsewhere (Chu et al., 1985; Bruck et al., 1989). All the correlations were performed using the commercial software, VIC-2D (Correlated Solutions, West Columbia, SC). The DIC technique allows the identification of non-local deformation fields and it was used to monitor the evolution of plastic deformation in closed-cell Al alloy foams upon quasi-static axial compression (Bastawros et al., 2000). Barthelat et al. (2003) extended this technique to dynamic testing, using images acquired by a high-speed camera. In the case of foams, the contours of the cells provided the dark and light patterns used in the correlation. From the full displacements fields computed by DIC, local nominal strains were determined. Additionally, the relative displacement of

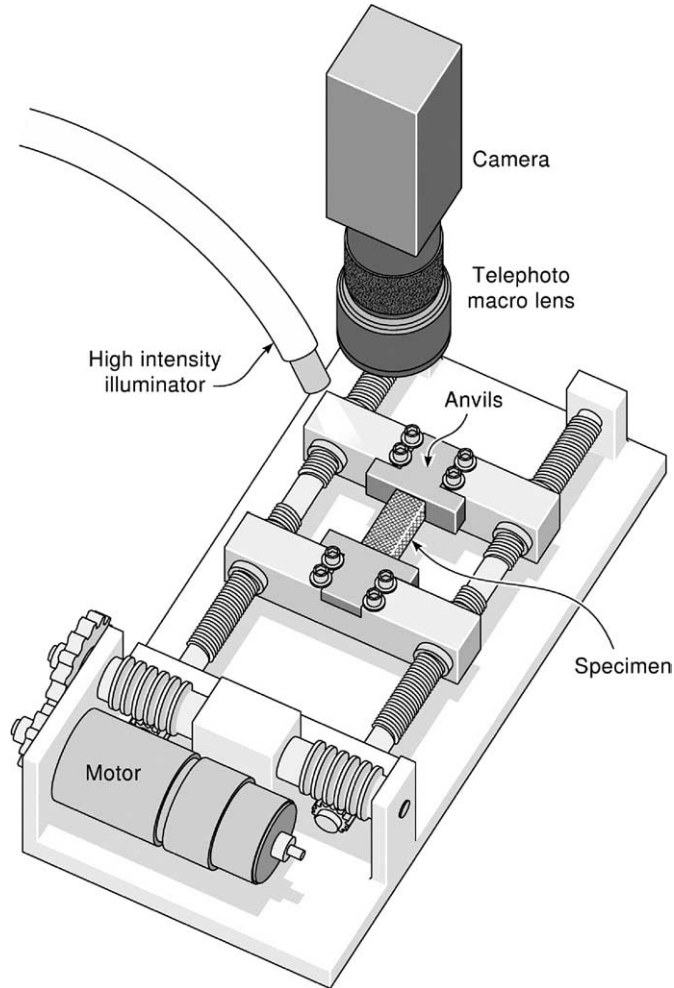


Fig. 1. Quasi-static compression test setup.

the two specimen boundaries was measured by DIC. This measurement provided the average nominal strain over the specimen as

$$\varepsilon_N(t) = \delta(t)/L_0 \quad (2)$$

where  $\delta(t)$  is the measured relative displacement and  $L_0$  is the initial length of the specimen. This optical method avoided complications due to loading stage compliance and specimen edge effects.

## 2.2. Kolsky bar experiments

For performing dynamic experiments at nominal strain rates in the range of  $100\text{--}1000\text{ s}^{-1}$ , a stored-energy Kolsky bar apparatus was used as shown in Fig. 2 (Espinosa and Nemat-Nasser, 2000; Espinosa et al., 2000). The apparatus consisted of two 1 in. diameter aluminum 7075-T6 bars mounted on linear bearings, between which a specimen was placed. To store the energy, the incident aluminum bar is clamped and a compressive load is applied using a hydraulic actuator. Upon release of the clamp, by fracturing a pin

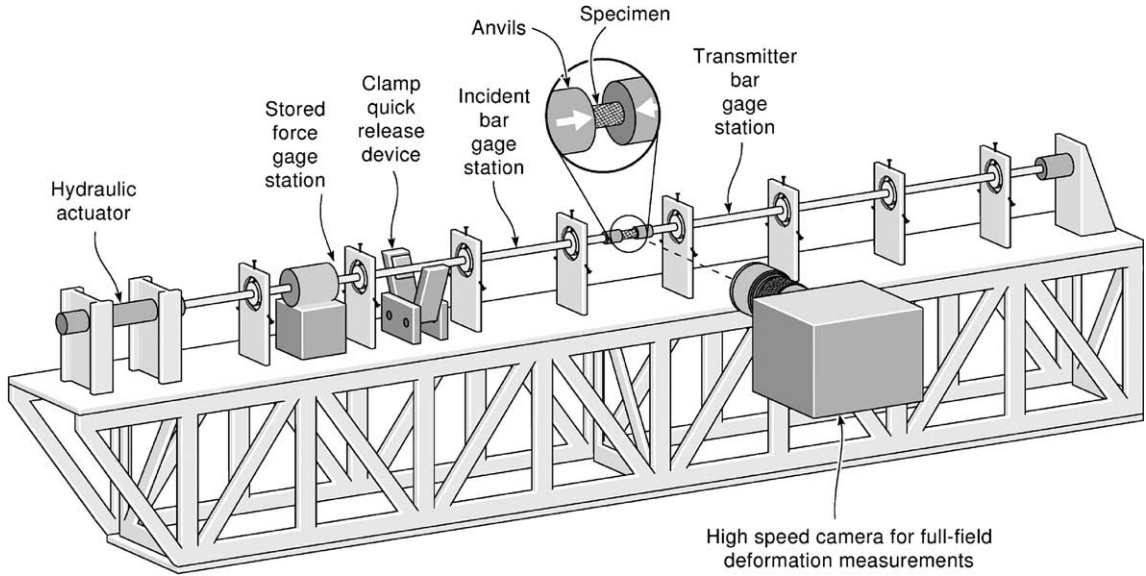


Fig. 2. Schematic of the Kolsky bar apparatus.

which holds the clamping force, a compressive stress wave travels down the bar into the specimen and the transmitter bar. Strain gage stations at different locations on the bars are connected to a signal conditioning and amplification system (Vishay Measurements Group, Inc., Raleigh, NC). An oscilloscope (Tektronix Inc., Beaverton, OR) was used to record incident, reflected, and transmitted pulses. Assuming elastic deformation in the pressure bars and force equilibrium at the two interfaces of the specimen, the force–time history applied to the specimen was computed from

$$F(t) = E_{Al} \frac{\pi D^2}{4} \varepsilon_t(t) \quad (3)$$

where  $E_{Al}$  is the Young's modulus of the aluminum employed in the pressure bars,  $D$  is the pressure bar diameter, and  $\varepsilon_t(t)$  is the strain history measured using a Wheatstone bridge at the strain gage station installed on the transmitter pressure bar. The overall deformation of the specimen is given by

$$\delta_N(t) = 2c_{Al} \int_0^t [\varepsilon_i(\tau) - \varepsilon_t(\tau)] d\tau \quad (4)$$

where  $c_{Al}$  is the sound speed in aluminum and  $\varepsilon_i(t)$  is the strain measured on the incident bar. The nominal stress was computed directly from Eqs. (3) and (1). The average nominal strain over the specimen was calculated directly by Eqs. (4) and (2) while the nominal strain rate was computed by differentiation of Eq. (4),

$$\dot{\varepsilon}_N(t) = 2 \frac{c_{Al}}{L_0} [\varepsilon_i(t) - \varepsilon_t(t)] \quad (5)$$

The incident pulse was also employed to trigger a high-speed eight CCD camera (Cordin, Salt Lake City, UT) equipped with a long distance microscope (Infinity, Boulder, CO). In the experiments later reported, the time interval between two frames was varied from 40  $\mu$ s to 80  $\mu$ s and the exposure time was set between 5  $\mu$ s and 20  $\mu$ s. Two halogen white light sources illuminated the specimen continuously. With appropriate synchronization the deformation history of the specimen can be observed on the eight images acquired by the high-speed camera. On the same sets of images, digital image correlation provides the full field

displacements with respect to the undeformed configuration (reference images which were taken before the test). We then follow the approach successfully implemented by Barthelat et al. (2003).

### 2.3. Gas gun experiments

Impact loading leading to higher nominal strain rates, up to  $10^4 \text{ s}^{-1}$ , were achieved using a 3 in. single stage gas gun apparatus (Fig. 3). The gas gun is composed of three main parts: a pressure chamber, a launching barrel, and a target chamber. Details of the design of the light gas gun can be found in Espinosa and Nemat-Nasser (2000). In the present study, a new setup illustrated in the Fig. 3(b) was developed to extend the rate of deformation achievable in the Kolsky bar while preserving the sample geometry and variables being monitored. In this setup, a *transmitter* bar was mounted on linear bearings in precise alignment with the gun barrel. In lieu of the incident bar, an impactor bar was employed, which was launched by the gas gun to apply dynamic loading onto the specimen. A sabot containing the impactor bar constituted the projectile, which was guided through the gun barrel by a keyway. A specimen was sandwiched between the transmitter and impactor bar.

The dimensions and materials of the impactor and transmitter bars were carefully determined to meet four specific conditions: (i) the deformations in the transmitter bar should remain in the elastic regime, (ii) the diameter of the transmitter bar and impactor should be the same, and small enough with respect to their length so that one-dimensional stress wave theory could be used in interpreting the experiments, (iii) the transmitter bar should have a length to fit in the target chamber, while the impactor bar should be short enough to be housed in a sabot while minimizing spurious motions, during the acceleration of the projectile, that could result in detrimental impact misalignments, and (iv) the pulse duration should be such that the specimen can reach significant compression before arrival of unloading waves from the free ends of the transmitter and impactor bars. According to one-dimensional stress wave theory, a 1-in. diameter aluminum 7075-T6 bar with length of 20 in. and a 1 in. diameter PMMA impactor with length of 10 in. met these design criteria. Fig. 4 shows a Lagrangian X–t diagram of the wave front in the PMMA impactor and aluminum transmitter bar upon impact.

PMMA was selected for its lower sound speed so that conditions (iii and iv) was satisfied with a short impactor. In addition, a range of impact velocity was chosen to achieve the nominal strain rate up to  $10^4 \text{ s}^{-1}$  and simultaneously to satisfy the conditions (i) and (iv) assuming that the specimen length is up to 1 in.

The impactor bar was mounted on an aluminum sabot 3 in. in diameter and 5 in. in length. PVC plates were glued at both ends of the sabot using five-minute epoxy. Those plates were designed to provide center-alignment to the impactor bar. In order to stop the sabot assembly, a gun barrel tubular extension was manufactured with the same inner diameter as the gun barrel. This self-aligning extension contained a retainer plate which was bolted to its end face. To prevent metal-to-metal contact resulting in large deformation of the Al sabot, a PVC foam ring (DIAB Inc., DeSoto, TX) 1 in. thick was mounted at the back of the retainer plate. The sabot reached this momentum-absorber ring only after full collapse of the specimen.

The specimen was mounted either on the transmitter bar (forward impact test) or on the PMMA impactor bar (reverse impact test, see Fig. 5). The strain history on the transmitter bar was recorded using a strain gage station mounted on the transmitter bar located 4 in. away from the specimen. The 4 in. distance is four times the pressure bar diameter, which is the minimum dimension to ensure that the propagating impact wave has reached equilibrium along the transmitter bar cross-sectional area. This gage location also maximizes the recording of the transmitted pulse (condition (iv)). The full bridge gage station was connected to the signal conditioner/amplifier and then to the oscilloscope. The strain history from the gage station was used to compute the load history applied to the specimen by means of Eq. (3).

In addition, optical measurements of projectile velocity and sample deformation rate were made *in situ*, by continuous and progressive blocking of a sheet of light in front of the transmitter bar and on top of the specimen location, see Figs. 3(c) and 6(a). The laser line velocity sensor (LLVS), originally developed by

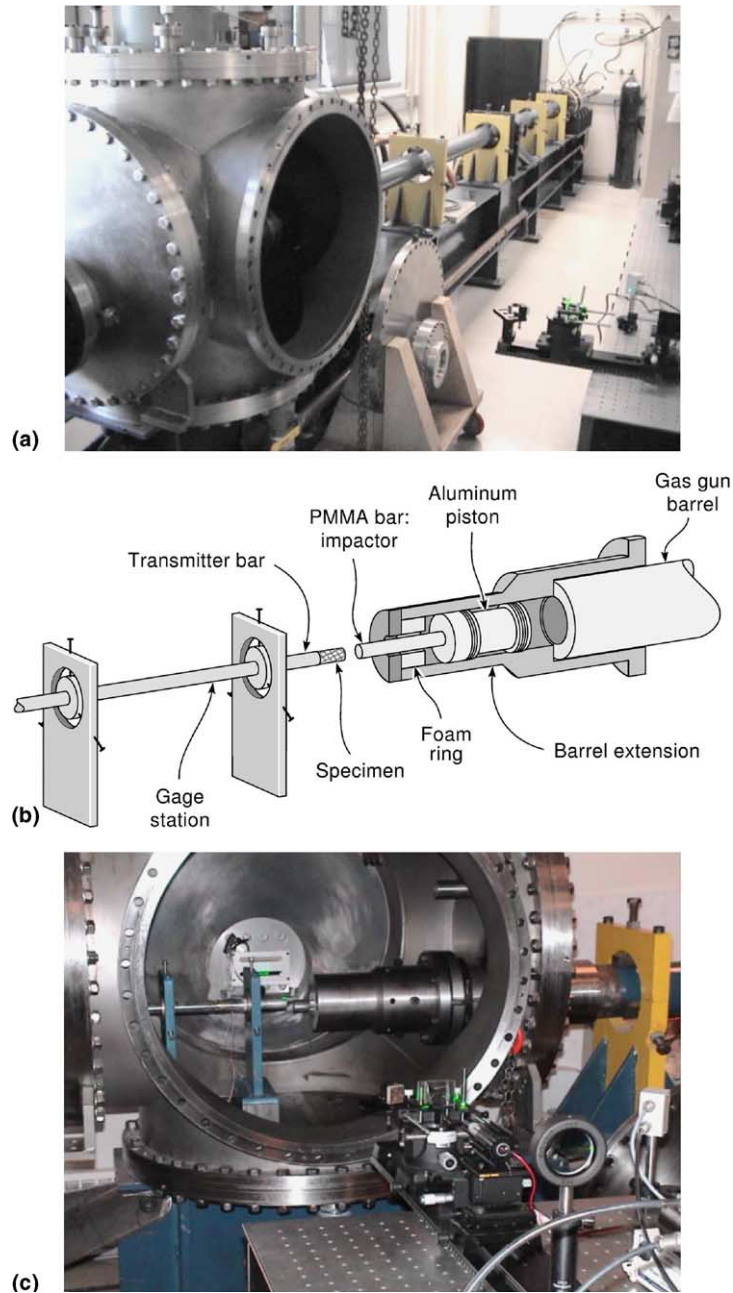


Fig. 3. (a) The light gas gun apparatus; (b) schematic of direct impact tests and new configuration for bar on bar impact; (c) target chamber and LLVS setup.

Ramesh and Kelkar (1995), was modified for this application such that the LLVS optics and photodetector are placed outside the target chamber. A 10 mW diode laser was combined with a collimating and line-generating optics to produce the sheet of light. The light sheet runs through the target chamber window and is

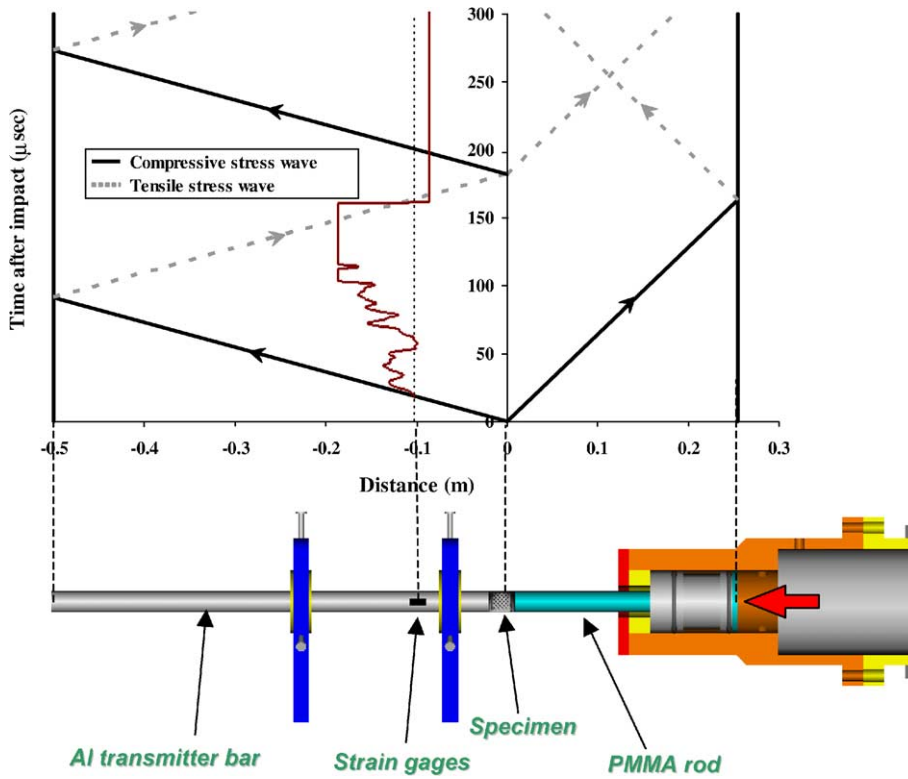


Fig. 4. Lagrangian diagram and wave profile in the transmitter bar.

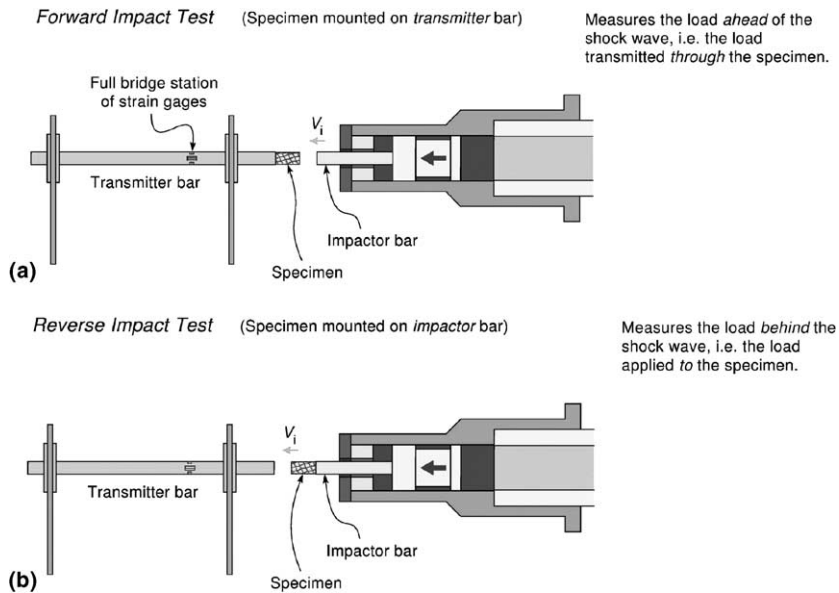


Fig. 5. Schematics of (a) forward impact and (b) reverse impact tests.

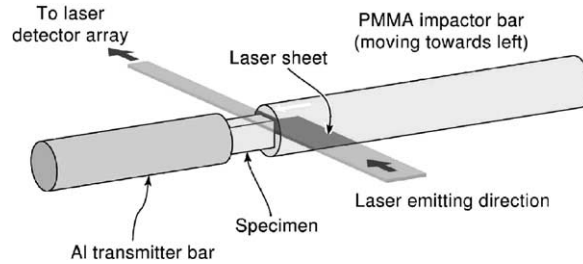


Fig. 6. Schematic of laser light sheet partially obstructed by the PMMA impactor.

reflected by a set of mirrors, to run back outside the chamber. The laser sheet is then focused on a photodiode by a collector lens. The optical setup is adjusted so that the PMMA impactor crosses the incident light sheet during the experiment. The corresponding drop in intensity at the photodiode can then be correlated, after calibration, with the position of the impactor. The signal is captured using an oscilloscope and the velocity history of the impactor is determined. The LLVS was shown to be an accurate, direct, continuous, and non-contact technique to measure velocities (Ramesh and Kelkar, 1995). In our case, the laser path was much longer than the setups of other researchers but the technique provided good estimates of the impact velocities as compared with a discontinuous measurement technique using images captured by the high-speed camera. The velocity of the impactor bar was used to compute displacements which in turn yielded the nominal strain in the specimen.

The signal from the LLVS was also employed to trigger the 8-CCD high-speed camera such that a series of images capturing the history of the specimen deformation were obtained. The time interval between each frame was varied from 10  $\mu\text{s}$  to 40  $\mu\text{s}$ . The typical exposure time was 5  $\mu\text{s}$ . A 5 W diode pumped laser (Coherent Inc., Santa Clara, CA) with a 2 in. beam expander was aimed at the specimen through the chamber window to provide diffuse and uniform illumination. The images were used not only to identify deformation and failure modes, but also to estimate the impact and crushing velocity.

The target chamber and launching barrel were evacuated to a pressure of approximately 40 Pa before the experiment to prevent the formation of a significant air cushion between the specimen and impactor (or transmitter bar) at impact. Nitrogen gas was pressurized into the pressure chamber at about 350 kPa, which upon release accelerated the projectile to about 100  $\text{m s}^{-1}$  through the launching barrel. During the test, but after specimen crushing, the nitrogen pressure was vented through lateral holes in the barrel extension. Likewise, the sabot was stopped by the rigid PVC foam ring and the steel retainer plate fastened onto the end of the barrel extension. The PVC back plate of the sabot failed as envisioned and allowed for the sliding of the PMMA impactor bar. This avoided additional specimen loading from the projectile assembly used to launch the impactor bar. These stages were essential to dissipate the remaining energy in the system and to recover the specimen, transmitter bar and aluminum piston without unintended damage.

### 3. Experimental results on aluminum foams

#### 3.1. Specimens

The metallic foam specimens used in this work were Duocel 6101-T6 aluminum alloy foam with open-cell architecture (ERG Materials and Aerospace, Oakland CA). The specimens had 7% relative density,  $\rho^*/\rho_s$  (the density,  $\rho^*$ , of the foam divided by that of the solid of which it is made,  $\rho_s$ ). The average cell size was

0.5 mm. Prismatic specimens were cut using water-jet in order to minimize cutting damage. The dimensions of the specimens were 25.4 mm × 17.78 mm × 17.78 mm for all the experiment presented in this work.

### 3.2. Effect of deformation rate

Fig. 7 shows nominal stress ( $F/A_0$ ) versus nominal strain ( $\delta/L_0$ ) plots for quasi-static and dynamic compression tests on the aluminum foam materials. The deformation rates ( $\dot{\delta}/L_0$ : nominal strain rate) measured in the experiments varied from  $7 \times 10^{-3} \text{ s}^{-1}$  for the quasi-static case and  $\sim 250 \text{ s}^{-1}$  for the Kolsky bar to  $2500\text{--}3300 \text{ s}^{-1}$  for the gas gun. The gas gun experiment was performed using the forward configuration, i.e., stationary specimen. All the curves show an initial stress build-up followed by a plateau stress of about 2.0–2.5 MPa. The quasi-static curve is monotonically increasing and densification is very progressive with a start at about  $\delta/L_0 = 0.4$ . The Kolsky bar experiments exhibit a peak stress with a minor nominal stress decay followed by a short plateau stress. Note that the duration of the pulse in the Kolsky bar was not enough to achieve significant specimen densification. In the case of the gas gun experiments, the initial slope of the nominal stress-nominal strain is lower than in the quasi-static and Kolsky bar experiments. Most likely, this is the case due to small misalignments between specimen and impactor bar. In these experiments, there is also a peak nominal stress followed by a progressive and small stress decay until densification at about  $\delta/L_0 = 0.6$ . The deformation rate has no significant effect on the plateau stress for any of the explored strain rates within material scatters. These results confirm the findings reported by [Dannemann and Lankford \(2000\)](#), and [Deshpande and Fleck \(2000\)](#). A difference between the quasi-static and gas gun experiments is the rate at which the stress changes with strain after densification initiates. The quasi-static curve shows a progressive increase in stress with gradual stiffening. By contrast the gas gun experiments show a much more stiff response during the final crushing stages. This is connected to the arrival of the crushing front to the transmitter bar as will be discussed later in the context of the formation of a crushing shock wave in the specimen.

Although the deformation rate ( $\dot{\delta}/L_0$ ) does not seem to have an effect on the overall compressive behavior of the aluminum open-cell foam specimens, it seems to control the foam cells deformation and failure modes. Differences in local strain fields were observed between quasi-static and Kolsky bar experiments. Fig. 8 shows snapshots of the specimen for both deformation regimes along with superimposed axial strain fields obtained by digital image correlation. It is observed that the deformations in the dynamic case are more distributed than in the quasi-static case. In the quasi-static case, the deformation is localized in

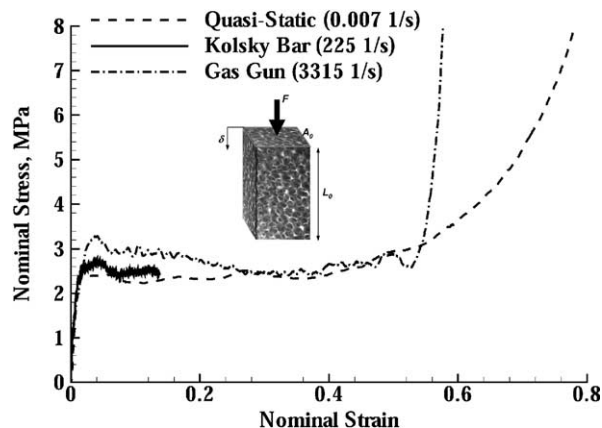


Fig. 7. Compressive stress–strain curves for an Al open-cell foam at various strain rates.

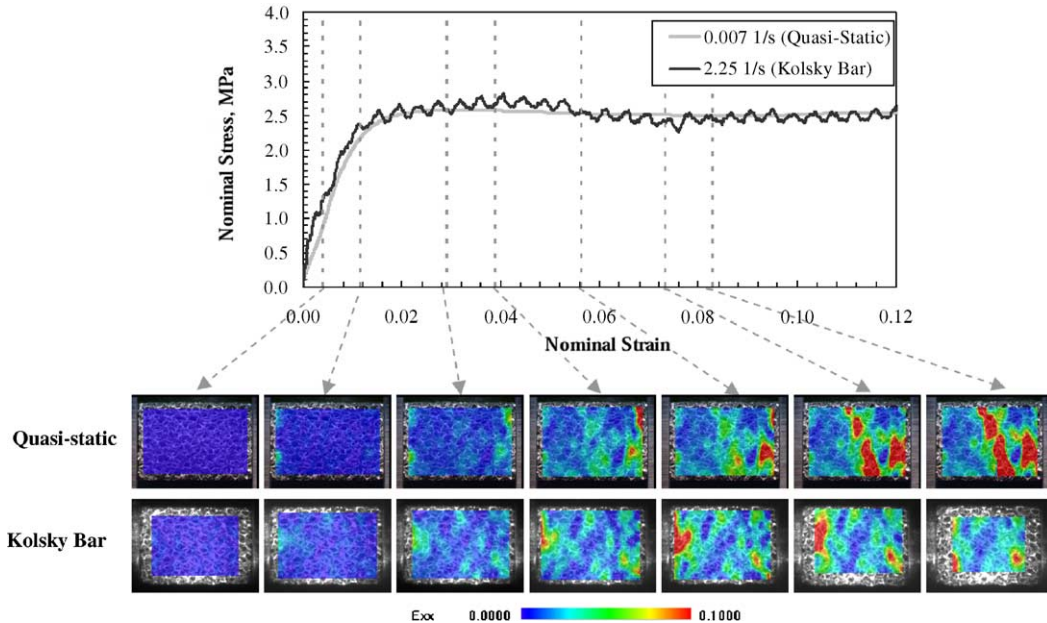


Fig. 8. Comparison of local deformation fields induced under quasi-static and Kolsky bar loadings. Al open-cell specimens.

one or two bands of collapsing cells, which is observed in closed-cell foams (Bastawros et al., 2000). The large deformations achieved in cell crushing involve significant displacement of material through bending and buckling of cell walls and ligaments. During high-rate dynamic loadings, we believe this motion is deterred by micro-inertia, and the result is that cell crushing tends to be more distributed. This phenomenon did not manifest itself in an appreciable increase in nominal crushing stress but the DIC analysis clearly shows that at the deformation rates achieved in the Kolsky bar experiments the specimen seems to offer more resistance to the development of strain localization due to the micro-inertia effect.

Fig. 9 shows a failure mode comparison between quasi-static and gas gun experiments. The stress was measured in front of the propagating shock wave (forward impact configuration). Consistent with wave propagation theory, the failure mode changes dramatically at the higher strain rates achieved in the gas gun. From the sequence of images shown in Fig. 9, a shock front propagates through the specimen until full specimen densification is observed. The foam collapses behind a leading shock front which is perpendicular to the loading axis and that propagates along the impact direction. Fig. 10 shows a deformation history of the foam in a forward impact test at a strain rate of  $3314 \text{ s}^{-1}$ . In this case, a longer exposure time of  $20 \mu\text{s}$  was employed for the high-speed camera shots. The blur and streaking on part of the image clearly show that the deformation is mostly concentrated behind the shock while the rest of the specimen seems almost undisturbed. The images also show that the front moves faster than the impactor as the volume of crushed cells expands. In order to measure the stress behind the crushing shock front, a reverse impact experiment was performed.

### 3.3. Reverse impacts

Behind the shock front, the effect of inertia is significant. Therefore, the forces at the two ends of the specimen are not equilibrated. In a reverse impact tests, the specimen is launched with the PMMA bar (see Fig. 4). As a result, the transmitter bar records the load history behind the shock front initiated at

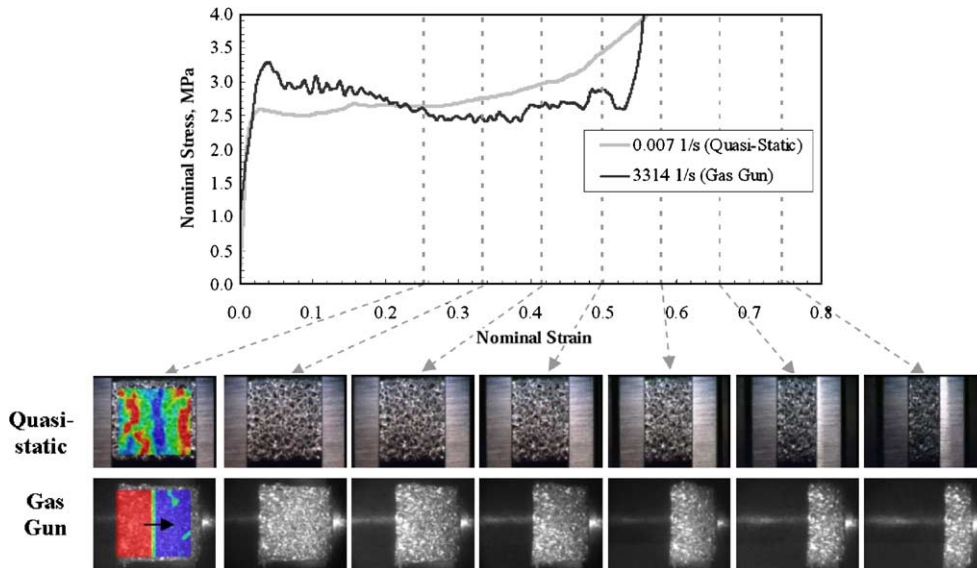


Fig. 9. Comparison of local deformation fields induced under quasi-static and gas gun loadings. Al open-cell specimens.

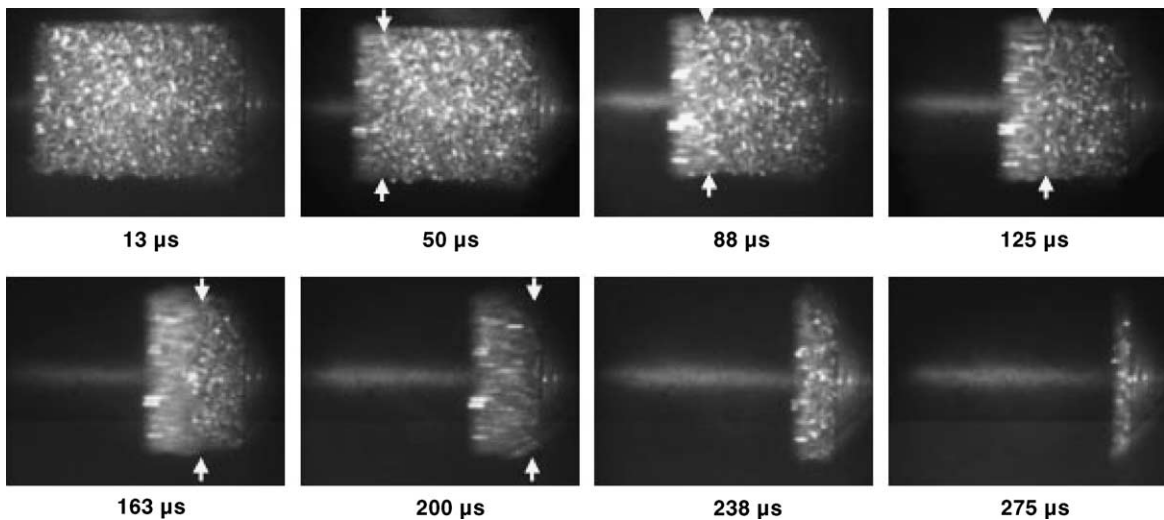


Fig. 10. Crushing front evolution as observed in gas gun impact experiments.

the impact surface. It implies that the reverse impact test measures the load applied to the crushing core while the forward impact test measures the load transmitted through the core. A comparison between forward and reverse impact results is shown in the Fig. 11. The average of the load measured in the reverse impact experiment is higher than that measured in the forward impact experiments. Considering the fact that these two tests were carried out at almost the same strain rate, it can be concluded that the load needed to crush the foam at high speeds of deformation is significantly higher than the load transmitted through

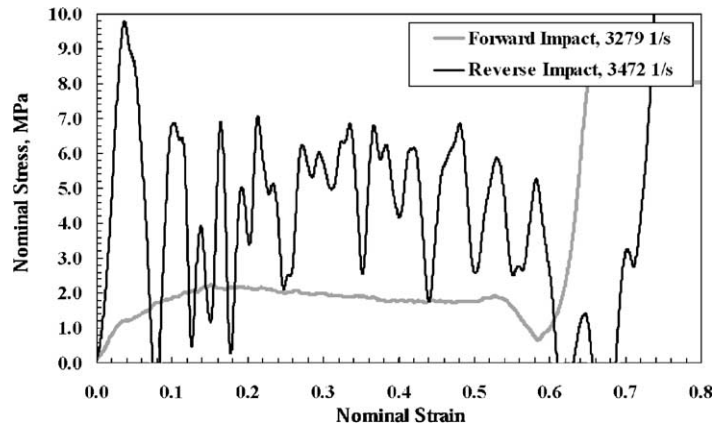


Fig. 11. Comparison between reverse and forward impact test results. Al open-cell specimens.

the foam. The fluctuations in the reverse impact test seem to be the result of local instabilities of cells clusters within the foam.

#### 4. Experimental results for woven textile lattice trusses

##### 4.1. Specimens

The 304 stainless steel woven textile core specimens were fabricated at University of Virginia. The details of fabrication were described in Sypeck and Wadley (2001), Wadley (2002), and Wadley et al. (2003). The relative density,  $\bar{\rho}$ , of the core was 12.6%. 304 SS wires of 0.508 mm diameter were woven into a layer which had diamond-shaped cells. The average cell size was 3.24 mm  $\times$  3.24 mm along the wires. The woven layers were stacked into 15.45 mm thickness. The thickness of the textile core in the loading direction was 17.63 mm and the width was 18.55 mm as shown in the Fig. 12.

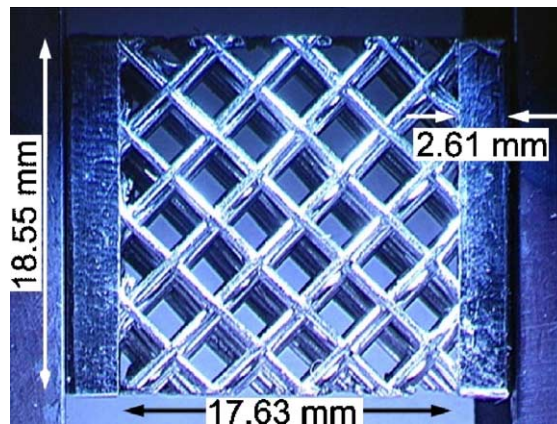


Fig. 12. The 304 stainless steel woven textile core specimen.

#### 4.2. Effect of deformation rates

The 304 stainless steel woven textile core specimens were compressed uniformly at different regimes of deformation rate in the range from  $0.007 \text{ s}^{-1}$  to  $5921 \text{ s}^{-1}$ . In quasi-static loading, the relative velocity between two compression platens was  $1 \times 10^{-4} \text{ m s}^{-1}$ , corresponding to a strain rate ( $\dot{\delta}/L_0$ ) of  $7 \times 10^{-4} \text{ s}^{-1}$ . The dynamic experiments were performed at a relative velocity of 4–6 m/s (deformation rate of  $230\text{--}330 \text{ s}^{-1}$ ) for the Kolsky bar tests and 72–104 m/s (deformation rate of  $4129\text{--}5921 \text{ s}^{-1}$ ) for the gas gun tests. Curves of nominal stress versus nominal strain for textile cores under different loading rates are given in Fig. 13. The curves show relative minor difference although appreciable across the explored deformation rates. The stress reaches a peak value after an initial elastic region and thereafter decays for a while and then progressively increases. In contrast to the open-cell foam signatures, the specimen behavior exhibits a progressive hardening associated with strain hardening. The initial peak stress increases with increase in deformation rate, but the area under the force–deformation curve, corresponding to the energy absorption, is much less sensitive to the loading rate. The rate sensitivity of the peak stress in the textile cores arises from the discreteness and robustness of the wires. In essence, its behavior is intermediate between open-cell foams and pyramidal truss cores as will be reported in a subsequent paper.

On the other hand, the failure mode has a well defined transition from quasi-static and Kolsky bar to gas gun. Fig. 14 shows captured images of the specimen corresponding to quasi-static and Kolsky bar tests along with superimposed  $x$ -direction strain field obtained by digital image correlation. For both quasi-static and Kolsky bar, the collapse occurs first on a plane at  $45^\circ$  along the specimen diagonal because of lack of lateral constraint. Thereafter, the collapse progresses to the adjacent cells and the number of truss lattices rotating and touching each other increases, which explains the macroscopic hardening of the material. As shown in Fig. 15, for the selected specimen dimensions, most wires are attached to only one face sheets. Hence, the absence of attachment promotes failure in shear and a few cross-braces prevent shearing in another direction. To avoid this edge effect, the specimen width should be much longer so that a plate aspect ratio (the width divided by the thickness in the loading direction) should exceed about 10 (Mumm et al., submitted for publication). The loading direction strain field of the quasi-static test exhibit more localized deformation in the diagonal row than the Kolsky bar tests. While this failure mechanism is dominant for quasi-static and Kolsky bar tests, the shear mode does not manifest itself in the gas gun experiments where a shock wave develops. As shown in Fig. 16, diamond-shaped cells adjacent to the impact surface collapsed first and the specimen is crushed along a plane parallel to the front face sheet. The shock front propagates

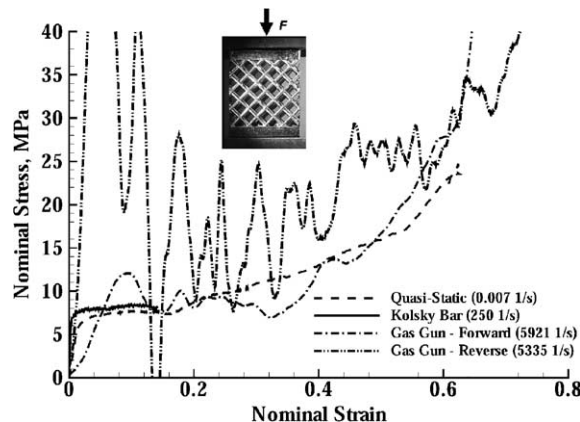


Fig. 13. Compressive stress–strain curves for the textile core specimen at various strain rates.

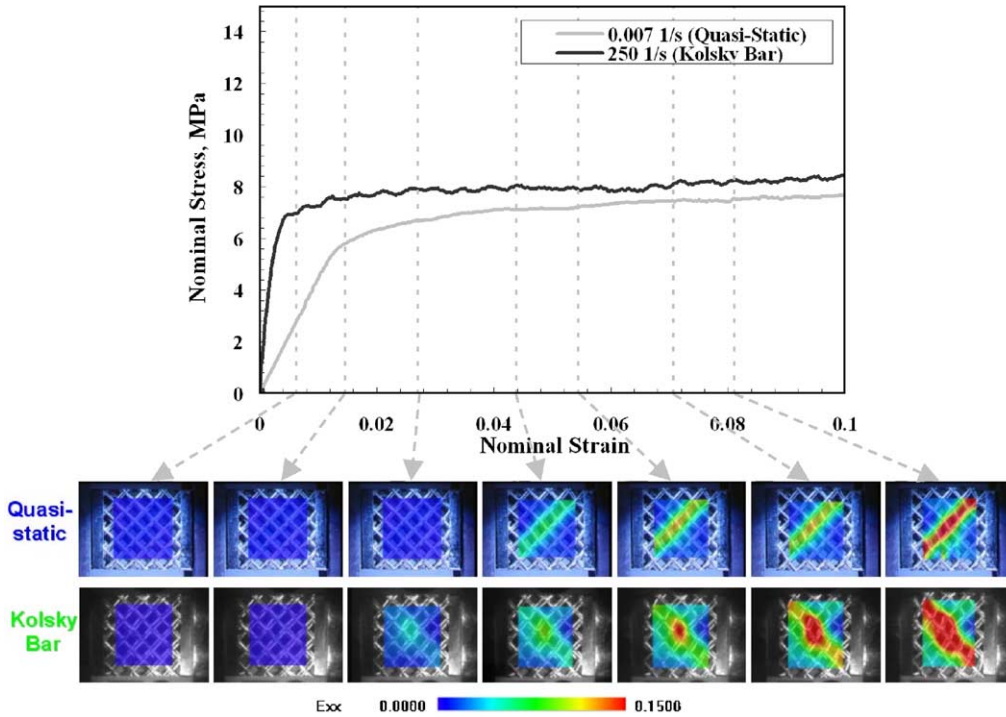


Fig. 14. Comparison of local deformation fields induced under quasi-static and Kolsky bar loadings. Textile core specimens.

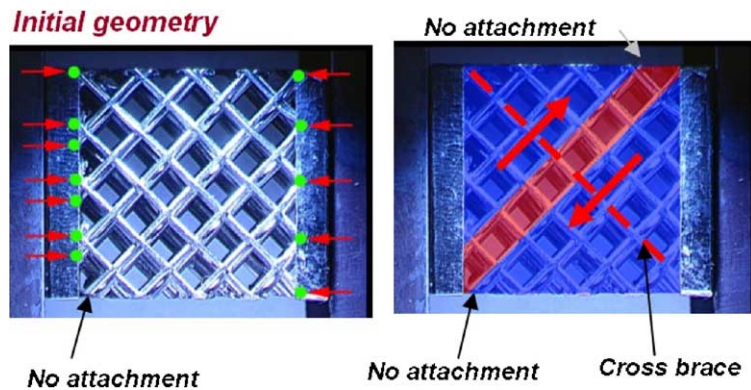


Fig. 15. Failure mode observed in quasi-static and Kolsky bar experiments. Textile core specimens.

through the specimen in the loading direction similarly to the shock front propagation in open-cell foams. It is interesting to observe that the stress–strain curves of gas gun tests dropped after the initial peak stress although they showed higher initial peak stresses than those of quasi-static and Kolsky bar tests. It is conjectured that the truss lattices next to the impact loading experienced instability because buckling of the truss lattices was required to crush the trusses initially and to generate a shock wave.

To measure the shock wave effect, reverse impact tests were carried out on the textile core specimens. In the preliminary tests, the mechanical impedance of the face sheet resulted in spurious overshooting peak

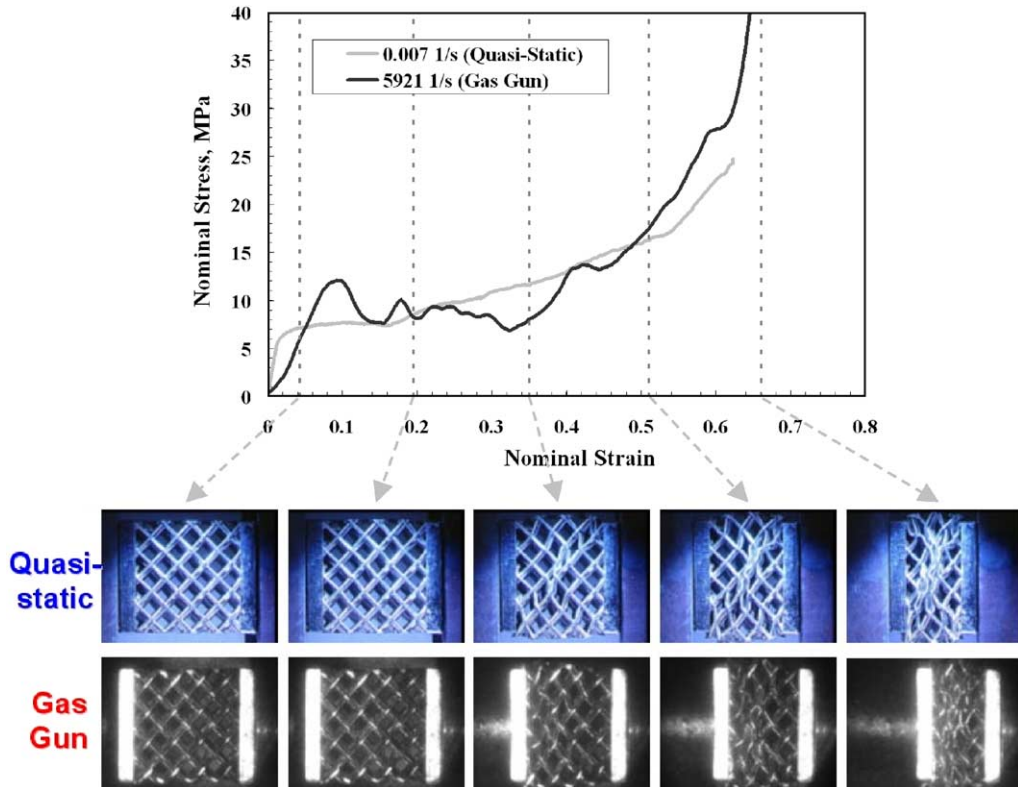


Fig. 16. Comparison of local deformation fields induced under quasi-static and gas gun loadings. Textile core specimens.

load and high-amplitude oscillations at the impact between the face sheet and the transmitter bar. The measured stress history is not only related to the behavior of the core but also to the wave structure within the impacting face sheet. Hence, to remove this effect as much as possible, the face sheet toward the impact surface was removed in the reverse impact experiments. Fig. 17 shows a comparison between forward and reverse impact results. Even after removing the face sheet, brazing material joining the core and the face sheet remained in gaps between ligaments. Therefore, the initial peak load was determined by this extra mass and associated inertia effect. The shock wave effect is clearly observed by the dash line fitted to an average stress. While this stress is higher than the one measured in the forward impact tests its evolution with nominal strain is similar. Again, the signal has many peak and valleys that may be attributed to a series of instabilities within the core.

## 5. Shock wave analysis

Structural shock waves have been shown to control the crushing behavior of cellular structural assemblies such as ring/tube systems, man-made honeycombs (Su et al., 1995a,b; Harrigan et al., 1999), and wood (Reid and Peng, 1997). The following presents a one-dimensional steady shock model to account for the inertia effects associated with the dynamic localization of crushing in foams during high-velocity impact compression.

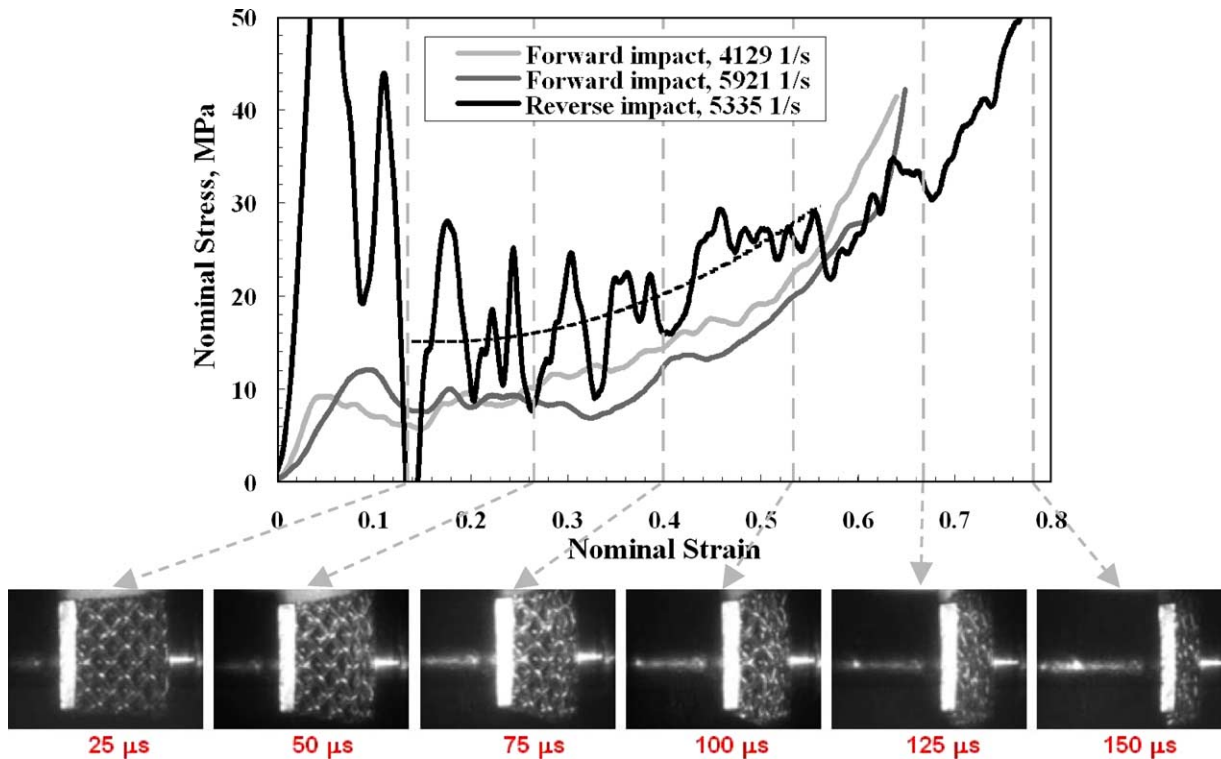


Fig. 17. Comparison between reverse and forward impact test results. Textile core specimens.

When a foam material is impacted at a sufficiently high velocity, a crushing front is initiated at the impact location and propagates through the material. The compressive stress behind this disturbance front greatly exceeds the plateau stress of the foam material. In this region, the cells have collapsed and the density is much larger than its initial value. In the remaining material, the deformation can be assumed to be essentially elastic with low particle velocity and density identical to its initial value. This traveling discontinuity of density and pressure follows the definition of a shock wave. Accordingly the Hugoniot–Rankine jump equation applies (Meyers, 1994). In the case of cellular materials, the Poisson's effect is negligible (no transverse stress) so one-dimensional stress wave propagation approximations can be used.

Following the model developed by Reid and Peng (1997) and Ashby et al. (2000), consider an idealized foam material assumed to follow a perfectly plastic locking behavior. The stress–strain curve for this material (Fig. 18) has no elastic deformation and follows a plateau stress  $\sigma_{pl}$ . Total cell collapse occurs at the densification strain  $\varepsilon_d$ . The material is then locked and no further deformation is allowed. The dash line in Fig. 18, connecting the stress state in front of and behind the shock, represents the so-called Rayleigh line and its significance will be discussed below.

A schematic of the shock wave propagating in a foam specimen under high strain rate deformation is shown in Fig. 19. Note that the schematic could correspond to either forward or reverse gas gun impact configurations and that the results of the model can be applied to both configurations. For simplicity, the model is presented for the case of a forward test where the left side of the specimen is in contact with the impactor bar and the right side is in contact with the transmitter bar. The values of mechanical impedances,  $\rho CA$  (multiplication of the material density,  $\rho$ , the sound speed in the material,  $C$ , and the area of impact surface,  $A$ ), for the impactor and the transmitter bar are significantly larger than that of the foam, so

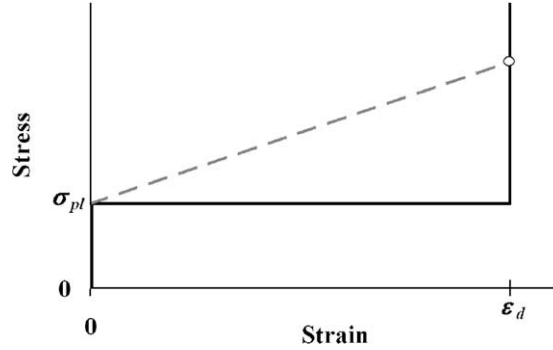


Fig. 18. Idealization of the nominal stress–strain curve for a metallic foam.

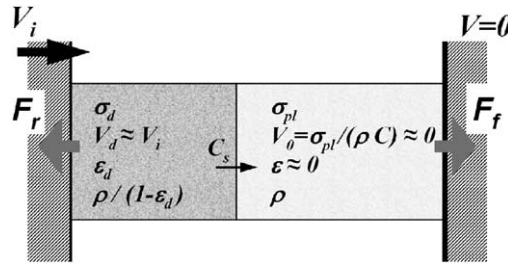


Fig. 19. Shock wave propagation and corresponding material states in front and behind the shock front for a foam specimen under direct impact.

they can be modeled as rigid masses. The impact velocity of the impactor  $V_i$  can therefore be assumed to be constant for the duration of the test, while the transmitter bar is assumed to be stationary.

Upon impact, elastic waves are generated within the specimen. A slower shock wave is generated and propagates through the material. Behind the shock wave, the material has collapsed and the strain is  $\epsilon_d$ . The particle velocity  $V_d$  in this region can be approximated to be equal to  $V_i$  and the stress  $\sigma_d$ , which is assumed constant is unknown. Ahead of the shock wave, the material is assumed to be at rest, with deformation  $\epsilon = 0$  and particle velocity  $V_0 = 0$ . This region is under a constant stress  $\sigma_{pl}$ . Under these conditions, conservation of mass across the shock front yields the relationship:

$$C_s = \frac{V_i}{\epsilon_d} \quad (6)$$

This equation provides the shock wave speed as function of impact velocity and material densification strain. The conservation of momentum provides the following equation:

$$\sigma_d - \sigma_{pl} = \rho C_s V_i \quad (7)$$

Eq. (7) relates the stress discontinuity across the shock wave to the impact velocity. Eqs. (6) and (7) yield the shock wave speed as function of the foam properties:

$$C_s = \sqrt{\frac{\sigma_s - \sigma_{pl}}{\epsilon_d \rho}} = \sqrt{\frac{E_t}{\rho}}, \quad \text{where } E_t = \frac{\sigma_s - \sigma_{pl}}{\epsilon_d} \quad (8)$$

Eq. (8) is similar in form to the classical definition of sound speed for a material. The tangential modulus  $E_t$  is the slope of the dash line in Fig. 18. This is the so-called Rayleigh line that connects the stress states behind and in front of the shock. Eliminating  $C_s$  from Eqs. (7) and (8) yields the stress in the compressed region, namely,

$$\sigma_d = \sigma_{pl} + \rho \frac{V_i^2}{\varepsilon_d} \quad (9)$$

The second term of the right hand side of Eq. (9) is the hydrodynamic term and characterizes the contribution of the shock wave to the increase in overall stress. In quasi-static loading this term vanishes. For the case of the forward gas gun experiment with  $V_i \sim 84 \text{ m s}^{-1}$ , the experimental plateau stress for the open-cell aluminum foam was  $\sigma_{pl} = 2.0 \text{ MPa}$ , while the densification strain was found at about  $\varepsilon_d = 0.6$ . The initial foam density was  $\rho = 189 \text{ kg/m}^3$  which gives a shock wave stress of  $\sigma_d = 4.2 \text{ MPa}$  more than twice of  $\sigma_{pl}$ . For this case, the hydrodynamic term represents 53% of  $\sigma_d$  showing that shock wave propagation governs the behavior of the specimen.

The model also predicts the critical impact velocity at which a shock wave develops. Assuming the onset of shock wave occurs when the hydrodynamic term contributes 10% of the static term  $\sigma_{pl}$ , the critical impact velocity generating a shock wave is

$$V_{ic} = \sqrt{0.1 \sigma_{pl} \frac{\varepsilon_d}{\rho}} = 33.5 \text{ m s}^{-1} \quad (10)$$

This value of  $V_{ic}$  is consistent with the experimental findings. In fact, the Kolsky bar experiments were performed at  $V_i = 6\text{--}7 \text{ m s}^{-1}$ . The value is well below  $V_{ic}$  and no shock wave was observed. On the other hand, the gas gun experiments were conducted at impact velocities of  $V_i = 60\text{--}85 \text{ m s}^{-1}$ . These values are above the critical value and shock waves were observed in the foam specimen in all gas gun experiments.

Finally, the model is used to compute the stress–strain curve of the foam specimen as obtained from a particular forward-impact test (load measured ahead of the shock wave) and by a reverse impact test (load measured behind the shock wave). Fig. 20 shows the idealized nominal stress–strain curves at both interfaces, based on the one-dimensional model, the experimental results. The model overall describes quite well the loads measured at both ends of the specimen. As previously mentioned, the reverse experiments result in a fluctuating stress history behind the shock wave, which results from details of the collapsing material. We attribute these fluctuations to a sequence of instabilities. Note that these details are not included in the

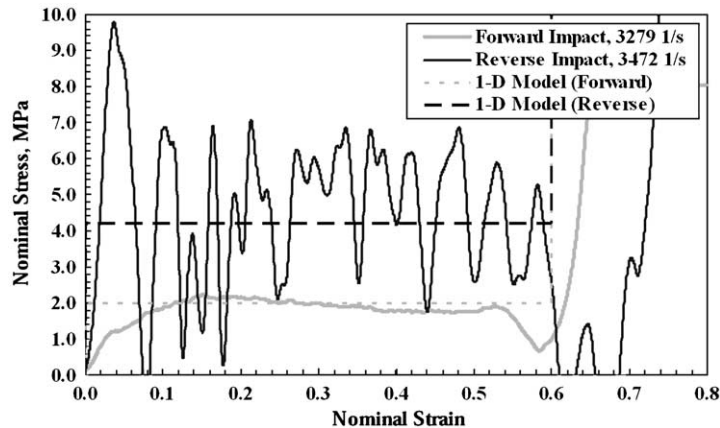


Fig. 20. Nominal stress–strain curves as predicted by the model for forward and reverse impact experiments and comparison with experimental results.

simplified model and as such only a constant average stress is predicted. The plots illustrate that the model is not accurate to capture stress history but it is quite useful in the prediction of energy absorbed by the material, see also Reid and Peng (1997) and Ashby et al. (2000).

## 6. Conclusion

The compressive behavior of open-cell aluminum foams and stainless steel textile cores was investigated, under various strain rates, using a unique combination of experiments. Quasi-static tests were performed using a miniature loading frame. A stored energy Kolsky bar was used for intermediate strain rates, while a light gas gun was used for direct and reverse impact of the specimens at high strain rates. Real time deformation observations were performed for all three test types. A digital CCD camera was used in quasi-static experiments and a high-speed camera with eight CCDs was employed in the dynamic experiments. The deformation modes could be investigated in detail from the images and digital image correlation.

For the case of open-cell foams, comparison between quasi-static and Kolsky bar experiments revealed moderate micro-inertia phenomena, where the inertia due to bending and buckling of the ligaments in the foam resisted strain localization. The gas gun experiments showed a totally different deformation mode due to a shock wave. A shock wave consisting of crushed material was generated at the impact surface and propagated through the specimen with a well-defined speed. By performing gas gun experiments in forward and reverse configurations, the stress levels in front and behind the crushing shock front were differentiated. The shock wave propagation was observed optically in *real-time*. When the quasi-static, Kolsky bar and forward gas gun experiments are compared, it is evident that the plateau or crushing stress is almost insensitive to strain rate.

A model based on one-dimensional shock wave theory on an ideal plastic locking foam material indeed predicted the formation of a shock wave above a critical value for the impact velocity. This value was consistent with the experimental measurements reported in this and previous work. The model was also used to predict the stress–strain curves as obtained by a forward and reverse impact experiment. Experimental measurements and theoretical predictions agree reasonably well specially in terms of energy dissipation. The reverse experiments show features associated to a series of instabilities with nominal stress increasing and decreasing rather than exhibiting a constant value as predicted by the model. However, the homogenized nominal stress level predicted by shock wave theory agrees well with the average of the nominal stress measured in the experiments.

In the case of textile cores, the findings were similar to the ones observed in open-cell foams. A well-defined failure mode transition was observed when the deformation rate was transitioned from  $500 \text{ s}^{-1}$  to  $1 \times 10^4 \text{ s}^{-1}$ . However, the peak stress was found to be deformation rate sensitive. In this regards, the textile cores exhibit an intermediate behavior between open-cell foams and pyramidal truss core cellular materials. At low strain rates, the collapse zone was observed in the central region with shear bands at  $\pm 45^\circ$  in orientation. At high strain rates, collapse occurred adjacent to the impact surface and propagated through the specimen in the direction of impact. The results, although representative of the material behavior, suffered from lack of lateral confinement due to the limited number of cells in the lateral direction. Future research should investigate specimens with a large number of cells across the width of the specimen so that the crushing stress determined in the experiments can be directly incorporated in constitutive models.

## Acknowledgements

This work was sponsored by the Office of Naval Research under Award No. 123163-02-N00014-02-1-0700. Special thanks are due to Professor J.W. Hutchinson from Harvard University and Professors

A.G. Evans and F. Zok, and Dr. H. Rathbun from University of California at Santa Barbara for their insightful discussions during the investigation reported here. The authors are also in debt with Drs. K. Dharmasena and D.T. Queheillalt from University of Virginia for their aid in fabrication of samples and helpful discussions.

## References

- Ashby, M.F., Evans, A.G., Fleck, N.A., Gibson, L.J., Hutchinson, J.W., Wadley, H.N.G., 2000. *Metal Foams—A Design Guide*. Butterworths-Heinemann, Woburn, MA.
- Barthelat, F., Wu, Z., Prorok, B.C., Espinosa, H.D., 2003. Dynamic torsion testing of nanocrystalline coatings using high-speed photography and digital image correlation. *Experimental Mechanics* 43 (3), 331–340.
- Bastawros, A.F., Bart-Smith, H., Evans, A.G., 2000. Experimental analysis of deformation mechanisms in a closed-cell aluminum alloy foam. *Journal of the Mechanics and Physics of Solids* 48 (2), 301–322.
- Bruck, H.A., McNeill, S.R., Sutton, M.A., Peters, W.H., 1989. Digital image correlation using Newton–Raphson method of partial differential correction. *Experimental Mechanics* 29, 261–267.
- Chu, T.C., Ranson, W.F., Sutton, M.A., Peters, W.H., 1985. Application of digital-image-correlation techniques to experimental mechanics. *Experimental Mechanics* 25, 232–244.
- Dannemann, K., Lankford Jr., J., 2000. High strain rate compression of closed-cell aluminium foams. *Materials Science and Engineering A* 293, 157–164.
- Deshpande, V.S., Fleck, N.A., 2000. High strain rate compressive behavior of aluminium alloy foams. *International Journal of Impact Engineering* 24, 277–298.
- Espinosa, H.D., Nemat-Nasser, S., 2000. Low-velocity impact testing. *ASM Handbook* 8, 539–559.
- Espinosa, H.D., Patanella, A., Fischer, M., 2000. A novel dynamic friction experiment using a modified Kolsky bar apparatus. *Experimental Mechanics* 40 (2), 138–153.
- Gibson, L.J., Ashby, M.F., 1997. *Cellular Solids, Structure and Properties*, second ed. Cambridge University Press, Cambridge, UK.
- Harrigan, J.J., Reid, S.R., Peng, C., 1999. Inertia effects in impact energy absorbing materials and structures. *International Journal of Impact Engineering* 22 (9–10), 955–979.
- Meyers, M.A., 1994. *Dynamic Behavior of Materials*. Wiley, New York.
- Mumm, D.R., Wei, Z., Evans, A.G., Sypeck, D.J., Wadley, H.N.G., submitted for publication. On the performance of light weight metallic panels fabricated using textile cores. *Journal of Applied Mechanics*.
- Ramesh, K.T., Kelkar, N., 1995. Technique for the continuous measurement of projectile velocities in plate impact experiments. *Review of Scientific Instruments* 66 (4), 3034–3036.
- Reid, S.R., Peng, C., 1997. Dynamic uniaxial crushing of wood. *International Journal of Impact Engineering* 19, 531–570.
- Su, X.Y., Yu, T.X., Reid, S.R., 1995a. Inertia-sensitive impact energy-absorbing structures. Part I: effects of inertia and elasticity. *International Journal of Impact Engineering* 16 (4), 651–672.
- Su, X.Y., Yu, T.X., Reid, S.R., 1995b. Inertia-sensitive impact energy-absorbing structures. Part II: effects of strain rate. *International Journal of Impact Engineering* 16 (4), 673–689.
- Sypeck, D.J., Wadley, H.N.G., 2001. Multifunctional microtruss laminates: textile synthesis and properties. *Journal of Materials Research* 16 (3), 890–897.
- Tam, L.L., Calladine, C.R., 1991. Inertia and strain-rate effects in a simple plate-structure under impact loading. *International Journal of Impact Engineering* 11 (3), 349–377.
- Tan, P.J., Harrigan, J.J., Reid, S.R., 2002. Inertia effects in uniaxial dynamic compression of a closed cell aluminium alloy foam. *Materials Science and Technology* 18 (5), 480–488.
- Wadley, H.N.G., 2002. Cellular metals manufacturing. *Advanced Engineering Materials* 4 (10), 726–733.
- Wadley, H.N.G., Fleck, N.A., Evans, A.G., 2003. Fabrication and structural performance of periodic cellular metal sandwich structures. *Composites Science and Technology* 63, 2331–2343.
- Yi, F., Zhu, Z., Hu, S., Yi, P., He, L., Ning, T., 2001. Dynamic compressive behavior of aluminium alloy foams. *Journal of Materials Science Letters* 20, 1667–1668.
- Yu, J.L., Wang, X., Wei, Z.G., Wang, E.H., 2003. Deformation and failure mechanism of dynamically loaded sandwich beams with aluminum-foam core. *International Journal of Impact Engineering* 28 (3), 331–347.
- Zok, F.W., Rathbun, H.J., Wei, Z., Evans, A.G., 2003. Design of metallic textile core sandwich panels. *International Journal of Solids and Structures* 40 (21), 5707–5722.
- Zupan, M., Deshpande, V.S., Fleck, N.A., 2004. The out-of-plane compressive behaviour of woven-core sandwich plates. *European Journal of Mechanics A—Solids* 23 (3), 411–421.